Chapter

Wake-Body Interaction Noise Simulated by the Coupling Method Using CFD and BEM

Masaaki Mori

Abstract

In many engineering applications, obstacles often appear in the wake of obstacles. Vortices shed from an upstream obstacle interact with downstream obstacle and generate noise, for example blades in a turbomachinery, tubes in a heat exchanger, rotating blades like a helicopter and wind turbine and so on. This phenomenon is called wake-body interaction or body-vortex interaction (BVI). The rod-airfoil and airfoil-airfoil configurations are typical models for the wake-body interaction. A rod and an airfoil are immersed upstream of the airfoil. In this chapter, we review the noise mechanism generated by the wake-body interaction and show the numerical results obtained by the coupling method using commercial CFD and acoustic BEM codes. The results show that depending on the spacing between the rod or airfoil and the airfoil, the flow patterns and noise radiation vary. With small spacing, the vortex shedding from the upstream obstacle is suppressed and it results in the suppression of the sound generation. With large spacing, the shear layer or the vortices shed from the upstream obstacle impinge on the downstream obstacle and it results in the large sound generation. The dominant peak frequency of the generated sound varies with increase in the spacing between the two obstacles.

Keywords: rod-airfoil configuration, airfoil-airfoil configuration, wake-body interaction, body-vortex interaction (BVI), coupling method, CFD, BEM

1. Introduction

Flow around a bluff body is one of the basic subjects in fluid mechanics, because it contains not only fundamentally important problems (such as forces acting on the body, transition to turbulence, acoustics, etc.), but also a variety of practical problems (such as structural design of buildings, trains, etc.). In many engineering applications, objects often appear in the wake of an obstacle. When an obstacle is in the wake of another, the flow structure tends to be complex and differs from that of single obstacle.

Flow past two circular or rectangular cylinders in a tandem arrangement is the simplified case of the flow past an array of cylinders and has received increasing attention [1–8]. Liu and Chen [4] and Inoue and Mori [5] showed that two different flow patterns appear depending on the space between the cylinders. When the

spacing is small, the shear layer separated from the upstream cylinder does not roll up to form vortices but reattaches to the downstream of the cylinder, and the vortices are shed from the downstream only, and this flow pattern is called *Mode I*. When the spacing is large, the shear layer separated from the upstream cylinder rolls up and forms vortices in front of the downstream of the cylinder, and the roll-up vortices impinge on the downstream cylinder (body-vortex interaction, BVI, wake-body interaction), and this flow pattern is called *Mode II*. Furthermore, Inoue and Mori [5] showed that in *Mode I,* the sound is generated only by the vortex shedding of the downstream cylinder, and in *Mode II,* the sound and strong pressure fluctuation around the downstream cylinder are generated mainly by BVI. The magnitude of the generated sound is much larger in *Mode II* than both *Mode I* and the single cylinder.

Since a *von Karman* vortex street can be regarded as a gust impinging on the obstacle or blade, a rod-airfoil model is another typical one for the study of the body (blade) vortex interaction or wake-body interaction. In this model, a rod is immersed upstream of the blade or airfoil, the wake formed behind the rod interacts with the leading edge of the blade or airfoil. Many studies concerned with the rod-airfoil model have been done both experimentally and numerically [9–21]. Jacob et al. [9] measured the flow field of the rod-NACA0012 airfoil model at the fixed spacing between the rod and the airfoil with varying the inflow velocity, and also measured the far field radiated noise spectra that are generated mainly by the body-wake interaction. They also performed numerical calculations using the Reynolds-averaged Navier-Stokes (RANS) and the large eddy simulation (LES) approaches and compared numerical results with the measured data. Munekata et al. [10–11] measured the flow field of the rod-airfoil model to research the effects of the spacing between the rod (cylinder) and the airfoil and the characteristics of the flow-induced sound generated by the flow around rod-airfoil. They showed that the roll up of the shear layer separated from the upstream rod is suppressed when the spacing between the rod and the airfoil is small, and the interaction between the wake from the rod upstream and the airfoil downstream becomes weak and it results in decreasing the level of the noise radiation. They also showed that the attack angle of the airfoil located downstream affects the characteristics of the flow-induced sound and wake structure at a given spacing between the rod and the airfoil, and the generated sound pressure decreases with the increase of the attack angle of the airfoil. Li et al. [12] performed the experiments of the body-wake interaction noise radiated from the flow around the rod-airfoil model by focusing on the noise control using "air blowing" on the upstream rod and a soft-vane leading edge on the airfoil. Numerical investigations by using the RANS approach have been done by Casalino et al. [13], Jacob et al. [9] and Jiang et al. [14], and those by using the LES approach have been done by Casalino et al. [13], Magagnato et al. [15], Boudet et al. [16], Jacob et al. [9], Greschner et al. [17], Agrawal and Sharma [18], Giret et al. [19], Daude et al. [20], and Jiang et al. [21]. Jiang et al. [21] performed LES simulations of the flow around the rod-airfoil for the inflow velocity U_∞ = 72 m/s and a Reynolds number based on the rod diameter (d) 48,000 (480,000 based on the airfoil chord, c) to clarify the flow patterns, velocity and pressure fluctuations, and noise radiation with varying the spacing between the rod and airfoil. They varied the spacing between the rod and the airfoil, such as L/d = 2, 4, 6, 8, and 10. They showed that when the spacing is small (L/d = 2), the vortex shedding of the rod upstream, the pressure fluctuation, and the noise radiation are suppressed as shown by Munekata et al. [10–11] and when the spacing is large (L/d = 6, 10), the pressure fluctuation, the noise radiation, and the fluid resonant oscillation due to the feedback loop between the rod and the airfoil become stronger.

The airfoil-airfoil model (airfoils in tandem) is also a typical model for the wake-body interaction or body-vortex interaction (BVI). Liu et al. [22–23] performed the measurements to understand the effect of using serration on the aerodynamic and acoustic performance of airfoils in tandem. They studied the wake development, static pressure distributions, and surface pressure fluctuations in detail for a cambered NACA 65-710 airfoil with and without the serration. They showed that the noise is reduced in the case that the upstream airfoil is with the serration.

In this chapter, we simulate the flow around the rod-airfoil model and the noise generated by the wake-body interaction or body-vortex interaction for the cases of L/d = 2 and 10 at a Reynolds number based on the rod diameter (d = 6 mm) 28,800 (288,000 based on the airfoil chord, c) by the coupling method using commercial CFD and acoustic BEM codes in which the acoustic sources are solved in the CFD code and the acoustic field is solved by means of BEM, and compare the results with those obtained by Jacob et al. [9] and Jiang et al. [21]. Then, we simulate the flow around the airfoil-airfoil model (airfoils in tandem) and the noise generation and propagation for the cases of L/c = 0.2, 0.6, and 1 at a Reynolds number based on the airfoil chord (c = 60 mm) 288,000, and compare the results with those for the rod-airfoil model.

2. Analysis model

2.1 Rod-airfoil flow model

A schematic diagram of the flow model is presented in **Figure 1**. The origin is at the leading edge of the airfoil. The coordinates parallel and normal to the free stream are denoted by x and y, respectively. The coordinate in the spanwise direction is denoted by z. The symbol L denotes the spacing between the rod and the airfoil. The lengths are made dimensionless by the rod diameter d and the velocity is scaled by the speed of sound c_∞. The normalized spacing L/d is prescribed to be 2 and 10. The Mach number, M, of a uniform flow is defined by $M = U_\infty/c_\infty$, where U_∞ denotes the velocity of the uniform flow. In this chapter, the Reynolds number is fixed to be Re_d = 28,800 or Re_c = 288,000, and those are based on the rod diameter and the airfoil chord c, respectively. The spanwise length of the rod and the airfoil is $3d$.

2.2 Airfoil-airfoil flow model

A schematic diagram of the flow model is presented in **Figure 2**. The origin is at the leading edge of the downstream airfoil. The normalized spacing L/c is

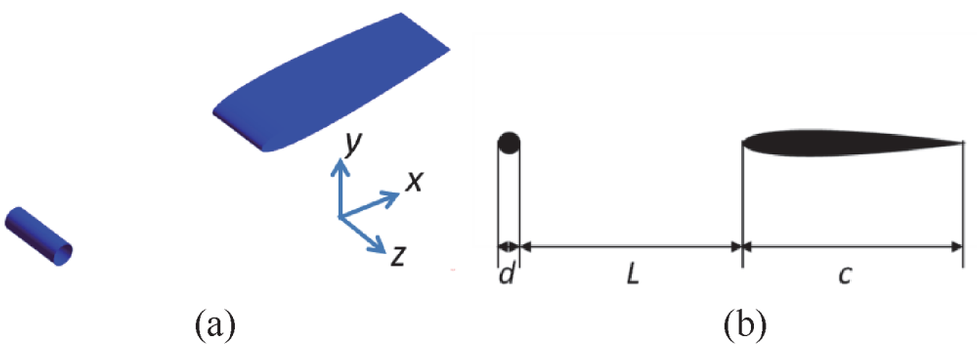

Figure 1.
Schematic diagram of rod-airfoil model. (a) Rod-airfoil model; (b) parameters.

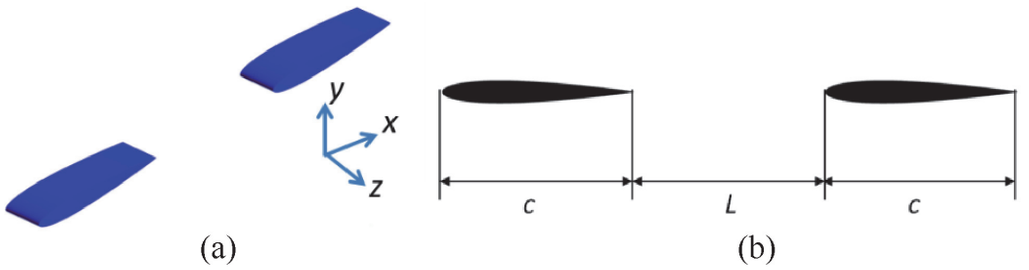

Figure 2.
Schematic diagram of arifoil-airfoil model. (a) Airfoil-airfoil model; (b) parameters.

prescribed to be 0.2, 0.6, and 1.0, and those are equal to L/d = 2.0, 6.0, and 10. In this chapter, the Reynolds number is fixed to be Re_c = 288,000, which is based on the airfoil chord c. The spanwise length of the airfoil and the airfoil is 0.3c, which corresponds to 3d.

3. Numerical procedure

3.1 Transient CFD simulation

Transient flow fields around rod-airfoil and airfoil-airfoil models are simulated at Reynolds number Re_d = 28,800 and Re_c = 288,000; those are based on the rod diameter and the airfoil chord, respectively. The inflow velocity in x direction, temperature, and density are U_∞ = 72 m/s, T_∞ = 300 K, and ρ_∞ = 1.177 kg/m^3, respectively and Mach number is M = 0.207. **Figure 3** shows a computational domain for the rod-airfoil and the airfoil-airfoil models. For these simulations, the three-dimensional computational domain has been applied, as shown in **Figure 3**. Unsteady flow fields are calculated using the commercial CFD code ANSYS Fluent version 2019R1 and its compressible LES (Dynamic Smagorinsky model) calculation features. Steady velocities are imposed on the inflow boundary. Pressure boundary conditions are applied on the top, bottom, and outflow boundaries. Non-reflecting boundary conditions are applied on top, bottom, inflow, and outflow boundaries. No-slip conditions are applied on the walls. At the boundaries at z = 0.009 m and − 0.009 m, the periodic conditions are applied.

The domains of the rod-airfoil simulation model contain 1,169,322 and 1,186,372 hex cells for L/d = 0.2 and 1.0, respectively. The domains of the airfoil-airfoil simulation model contain 1,423,114; 1,435,343; and 1,434,356 hex cells for L/c = 0.2,

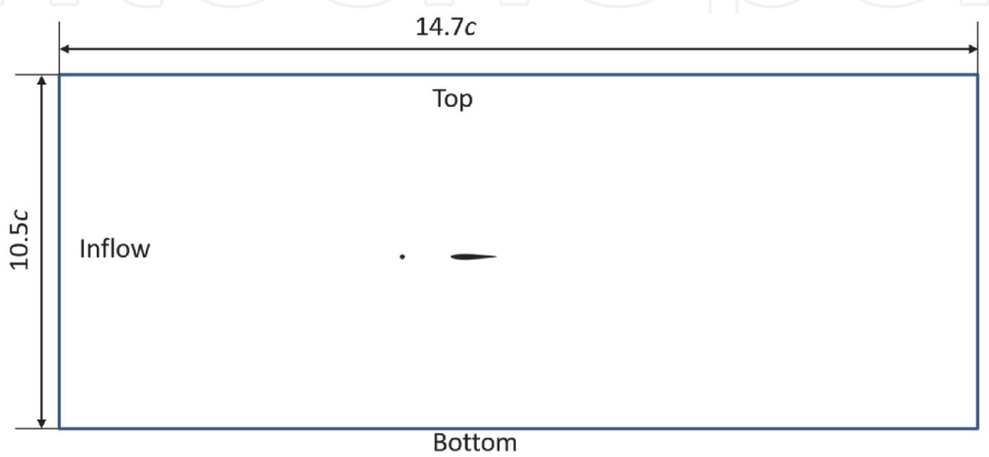

Figure 3.
Computational domain.

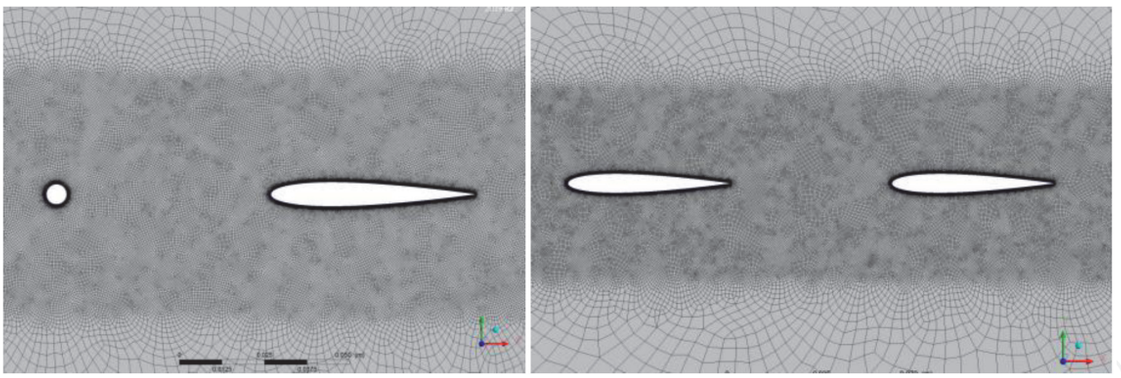

Figure 4.
Computational mesh. (a) Rod-airfoil model; (b) airfoil-airfoil model.

0.6, and 1.0, respectively. **Figure 4(a)** and **(b)** shows the computational meshes near the rod-airfoil and the airfoil-airfoil models, respectively. The cell spacing adjacent to the wall is 0.2 mm ($0.033d$). Steady-state simulations were performed using Spalart-Allmaras (S-A) turbulence model and then used as initial conditions of transient LESs. The transient simulations were performed for 50,000 time steps with a time step size Δt = 2e-6 s.

3.2 Lighthill equation

Lighthill equation [24, 25] in the frequency domain is derived from the equation of continuity and compressible Navier-Stokes equation and as follows:

$$\left(\nabla^2 + k^2\right)p = -\frac{\partial^2 T_{lm}}{\partial x_l \partial x_m} \tag{1}$$

where p is the acoustic pressure, k is the wave number, c_∞ is the speed of sound, l and m indicate each direction in the Cartesian coordinates, and v is the flow velocity. T_{lm} is the Lighthill stress tensor and as follows:

$$T_{lm} = \rho v_l v_m + \left(p - {c_\infty}^2 \rho\right)\delta_{lm} - \tau_{lm}, \tag{2}$$

where ρ is the density and is 1.225 kg/m3, δ_{ij} is the Kronecker delta, and τ_{lm} is the viscous stress tensor. For a low-Mach number and high-Reynolds number flow regime, the second and third terms of Eq. (2) are negligible [26–29]. Therefore, the first term is used for the present work.

3.3 Extraction of acoustic source

To convert the acoustic source time histories into the frequency spectra, the discrete Fourier transform (DFT) has been applied. The acoustics sources are extracted from 1250 steps (from t = 0.05 s to 0.1 s) flow field data, the sampling period is 4e-5 s.

3.4 Acoustic simulation

The BEM solver in commercial acoustic simulation package, WAON, is used to solve the acoustic characteristics [30]. In a sound field that satisfies the three-dimensional Helmholtz equation, the Kirchhoff-Helmholtz integral equation [31]

for sound pressure is described as follows with respect to a point i and an area S of a surface on a boundary.

$$\frac{1}{2}P(\boldsymbol{r}_i) = \int_{\Gamma}\left(P(\boldsymbol{r}_q)\frac{\partial G(\boldsymbol{r}_i,\boldsymbol{r}_q)}{\partial n_q} - \frac{\partial P(\boldsymbol{r}_q)}{\partial n_q}G(\boldsymbol{r}_i,\boldsymbol{r}_q)\right)dS + p_d(\boldsymbol{r}_q) \tag{3}$$

In this solver, the following simultaneous linear equation is solved:

$$(\boldsymbol{E}+\boldsymbol{B}+\boldsymbol{C})\boldsymbol{p} = j\omega\rho\boldsymbol{A} + \boldsymbol{p_d} \tag{4}$$

Here, p is the acoustic pressure vector, v is the particle velocity vector, and the entries of the influence coefficient matrices are represented as follows:

$$E_{ij} = \frac{1}{2}\delta_{ij}, \tag{5}$$

$$A_{ij} = \int_{\Gamma_1} N_j(\boldsymbol{r}_q)G(\boldsymbol{r}_i,\boldsymbol{r}_q)dS_q, \tag{6}$$

$$B_{ij} = \int_{\Gamma} N_j(\boldsymbol{r}_q)\frac{\partial G(\boldsymbol{r}_i,\boldsymbol{r}_q)}{\partial n_q}dS_q, \tag{7}$$

$$C_{ij} = \frac{jk}{Z_j}\int_{\Gamma_2} N_j(\boldsymbol{r}_q)G(\boldsymbol{r}_i,\boldsymbol{r}_q)dS_q, \tag{8}$$

$$G(\boldsymbol{r}_i,\boldsymbol{r}_q) = \frac{e^{jk|\boldsymbol{r}_p-\boldsymbol{r}_s|}}{4\pi|\boldsymbol{r}_p-\boldsymbol{r}_s|} \tag{9}$$

where δ_{ij} is Kronecker delta, and Γ_1 is a vibration boundary and a part of Γ. Γ is the total boundary. Γ_2 is an absorption boundary and a part of Γ. $\boldsymbol{r_i}$ is the position vector at the node i, $\mathbf{r_q}$ is the position vector of the source point q, and N_j is the interpolation function of the node j. z_j is the acoustic impedance ratio at the node j. G is the fundamental solution of a three-dimensional sound field. With the number of nodes N, the component p of the vector $\boldsymbol{p}$ is expressed as follows:

$$p(\boldsymbol{r}_q) = \sum_{j=1}^{N} N_j(\boldsymbol{r}_q)p_j. \tag{10}$$

The component p_d of the vector $\boldsymbol{p_d}$ is the direct pressure contribution from the acoustic source, which is evaluated by the following equation:

$$p_{\mathrm{d}}(\boldsymbol{r}_{\mathrm{p}}) = \frac{1}{4\pi}\frac{\partial^2}{\partial x_l \partial x_m}\int_{-\infty}^{\infty}\frac{T_{lm}(\boldsymbol{r}_s,\omega)e^{jk|\boldsymbol{r}_p-\boldsymbol{r}_s|}}{|\boldsymbol{r}_p-\boldsymbol{r}_s|}dV \tag{11}$$

where $\partial^2/\partial x_l \partial x_m$ is the directional derivative and V is the volume of the flow field (in this case, the region filled by CFD cell). $\boldsymbol{r_p}$ is a position vector of the monitor point p, and $\boldsymbol{r_s}$ is a position vector of the source point s. There are 8340 boundary elements. The acoustic sources are extracted from CFD results, whose numbers are equivalent to the number of grids of the CFD model. **Figure 5** shows the boundary elements.

3.5 Validation of numerical results

The numerical accuracy of the computation has been examined for the case of L/d = 10 in the rod-airfoil model. In order to validate the present computation, we

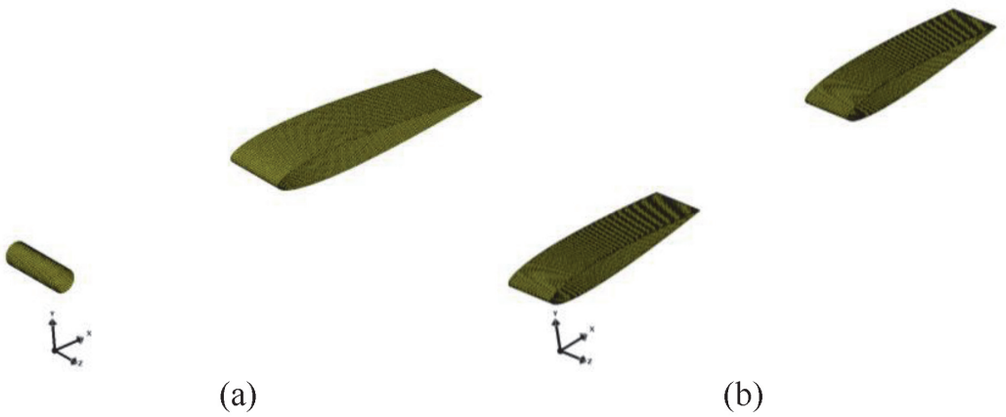

Figure 5.
Boundary elements. (a) Rod-airfoil model; (b) airfoil-airfoil model.

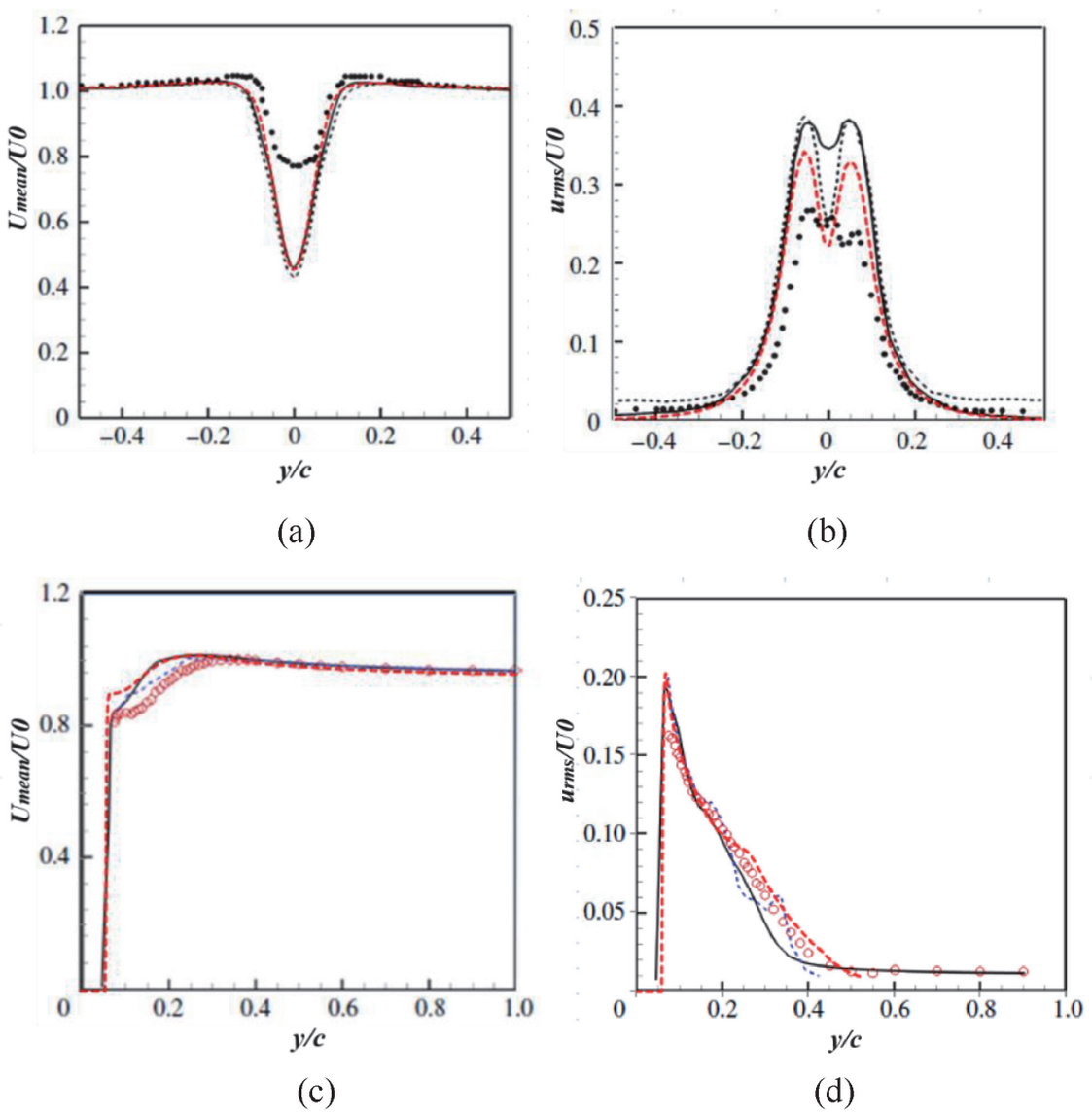

Figure 6.
Mean velocity and RMS of fluctuation velocity in x *direction distributions at* x/c = −0.87 *(a), (b) and* 0.25 *(c), (d). (a) Velocity; (b) RMS value of fluctuation velocity.* •••••• *Measured by Jacob et al. [9]* (Re_d = 48,000); ····· *Agawal and Sharma [18]* (Re_d = 48,000); ——— *Jiang et al. [21]* (Re_d = 48,000); – – – *present* (Re_d = 28,800). *(c) Velocity; (d) RMS value of fluctuation velocity.* ····· *Measured by Jacob et al. [9]* (Re_d = 48,000); - - - - *Boudet et al. [16]* (Re_d = 48,000); ——— *Jiang et al. [21]* (Re_d = 48,000); – – – *present* (Re_d = 28,800).

compared the present results with the experimental measurements performed by Jacob et al. [9] and the numerical results performed by Boudet et al. [16], Agawal and Sharma [18], and Jiang et al. [21], respectively. However, it is specified that the present study is performed at Re_d = 28,800, d = 0.06 m, and other experiments and the simulations are performed at Re_d = 48,000, d = 0.1 m. **Figure 6** shows the mean velocity and RMS value of the fluctuation velocity in x (streamwise) direction normalized by the incoming velocity at two locations x/c = −0.87 and x/c = 0.25. As shown in **Figure 6(a)**, the present calculation predicted similar mean velocity profile in the streamwise direction compared with other numerical results. As shown in **Figure 6(b)**, the RMS value of the fluctuation velocity in the streamwise direction obtained by the present calculation is close to those obtained by the other numerical calculations; however, the difference of the fluctuation velocity near the center-line can be seen. A possible cause for this result is the difference of the methods, meshes and Reynolds number. **Figure 6(c)** and **(d)** shows that the calculated profiles of the mean velocity and the RMS of the fluctuation velocity in the streamwise direction represent a good agreement with those from the experiments and other numerical results.

Figure 7 shows the spectra of the SPL at the location (x = 0.68 m, y = 1.74 m) calculated by the acoustic BEM simulation using the acoustic sources extracted from the CFD results. The peak frequency (St 0.2) and the spectrum around the peak frequency are well predicted compared with the experimental result obtained by Jacob et al. [9]. The peak value of the SPL obtained by the present study is slightly lower than that from the experimental result. There is a difference in the spectrum at high frequencies, St > 0.6. A possible cause for these differences of the peak SPL and the spectrum at high frequencies is that the Reynolds number is different between the present study and the experiments, and the mesh and time resolutions for the calculation might not be enough for the accurate prediction of the spectrum at high frequencies. However, the dominant peak SPL and SPLs around the peak frequency are well predicted in the present calculation. The peak frequency St 0.2 as shown in **Figure 7** almost corresponds to the vortex shedding frequency of the cylinder [2], which means that the vortex shedding from the rod plays an important role for the noise generation from the rod-airfoil model.

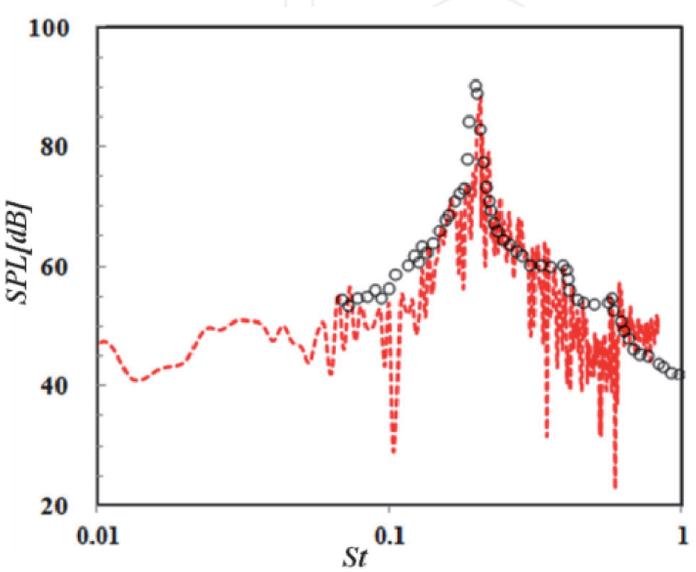

Figure 7.
SPL spectra at the location x = *0.68 m,* y = *1.74 m.* • • • • • *Measured by Jacob et al. [9]* (Re_d = *48,000);* – – – *present* (Re_d = *28,800).*

4. Results

4.1 Rod-airfoil simulation results

4.1.1 Flow patterns

Typical examples of instantaneous vorticity fields are presented in **Figure 8**. In the present calculation, for the case of L/d = 2, when the spacing between the rod and the airfoil is small, the boundary layers separated from the rod upstream did not roll up and reattaches to the airfoil downstream. The shear layers rolled up and formed vortices on the downstream airfoil surface, and the vortices were shed and convected downstream. The Kármán-vortex street formed from the rod was suppressed for the short spacing, and this mode is called "non-shedding mode" and "the Kármán-vortex street suppressing mode" as indicated by Munetaka et al. [10] and Jiang et al. [21], respectively. On the other hand, for the case of L/d = 10, when the spacing between the rod and the airfoil is large, the boundary layers separated from the rod upstream rolled up and formed vortices in the region between the rod and the airfoil, and the formed vortices shed from the rod interacted with the airfoil and impinged on the leading edge of the airfoil. The impinged vortices were distorted and convected downstream. This mode is called "the Kármán-street shedding mode" as indicated by Jiang et al. [21], and also called wake-body interaction or body-vortex interaction [6, 16, 21]. Similar phenomena such as the

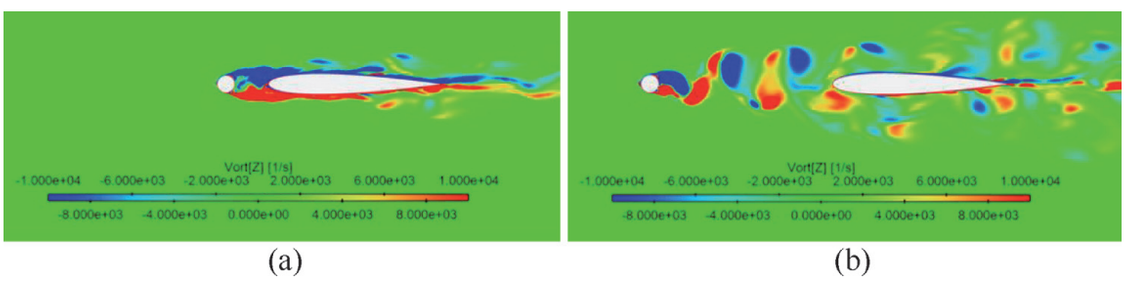

Figure 8.
Vorticity in the z direction. (a) L/d = *2; (b)* L/d = *10.*

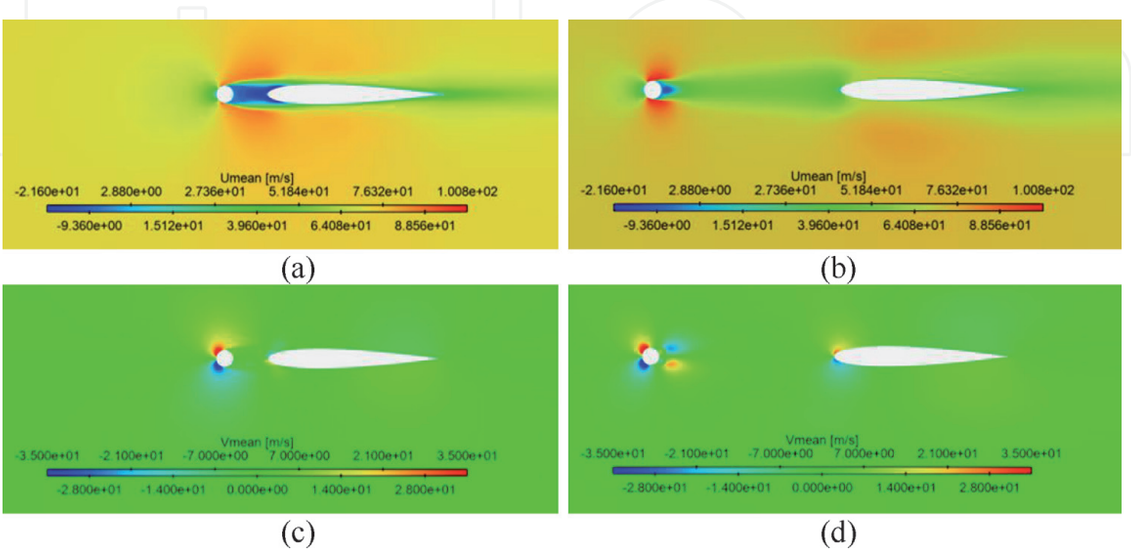

Figure 9.
Time-averaged velocity in the streamwise (x) *and the vertical* (y) *directions. (a), (b) velocity in the streamwise* (x) *direction; (c), (d) velocity in the vertical* (y) *direction. (a)* L/d = *2; (b)* L/d = *10; (c)* L/d = *2; (d)* L/d = *10.*

Kármán-street shedding and suppressing modes can be seen in the flow around two obstacles in tandem [2, 4, 6].

Figure 9(a) and **(b)** shows the fields of time-averaged velocity U_{mean} in the x (streamwise) direction. In the space between the rod and the airfoil, **Figure 9(a)** shows that the counter-rotating vortices near the leading edge of the airfoil lead to very small or negative values of U_{mean} for the case of L/d = 2. The reattachments of the counter-rotating vortices to the leading edge of the airfoil due to the approaching rod slow down the flow. By contrast, for the case of L/d = 10, the flow behind the rod was accelerated in front of the leading edge of airfoil as shown in **Figure 9(b)**.

Figure 9(c) and **(d)** shows the fields of time-averaged velocity V_{mean} in the y (vertical) direction. For the case of L/d = 2, the positive V_{mean} appears in the $-y$ region around the leading edge of the airfoil and the negative one appears in the opposite region. This is due to the reattachments of the negative and positive vortices formed from the rod upstream. For the case of L/d = 10, the V_{mean} distribution in the regions around the leading edge of the airfoil is contrary to that for the case of L/d = 2, as shown in **Figure 9(c)**. This phenomenon is indicated by Jiang et al. [21].

Finally, the fields of RMS value of the fluctuation velocity u_{rms} in the streamwise (x) direction are represented in **Figure 10** for L/d = 2 and L/d = 10. As shown in **Figure 10**, for the case of L/d = 2, the u_{rms} values behind the rod and near the central line y = 0 are much lower than those for the case of L/d = 10. This result corresponds to the suppression of the Kármán-vortex street for the case of L/d = 2 in the rod-airfoil model, and the reattachment of the main separated vortices to the airfoil (see **Figure 8**) causes the very small or negative U_{mean} generated in the space between the rod and the airfoil (see **Figure 9(a)**) in this case. On the other hand, in the case of L/d = 10, the u_{rms} values behind the rod and around the airfoil are much larger than those for the case of L/d = 2. Therefore the turbulent fluctuations in the space between the rod and the airfoil for the case of L/d = 10 seem to be much larger than those for the case of L/d = 2.

4.1.2 Near pressure field

Instantaneous snapshots of static pressure and snapshots of mean pressure are represented in **Figure 11**. For the case of L/d = 2, **Figure 11** shows that the value of the static pressure on the upstream side of the rod is larger than that on the downstream side, and that on the leading edge of the airfoil is negative and much lower than that for the case of L/d = 10.

Figure 12 shows the mean pressure distribution on the surface of rod and the airfoil, where x_{rod} is the coordinate in the streamwise direction and the origin of x_{rod} is the located in the stagnation point of the rod. Depending on the spacing between the rod and the airfoil, the pressure behind the rod is affected by the airfoil [21]. For

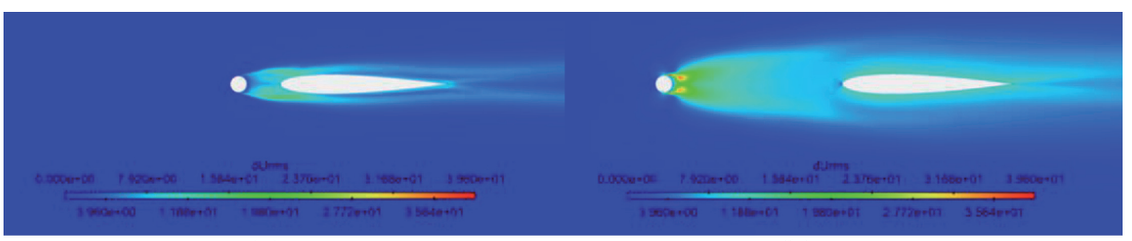

(a) (b)

Figure 10.
*RMS value of fluctuation velocity in the streamwise (*x*) direction. (a)* L/d = 2*; (b)* L/d = 10*.*

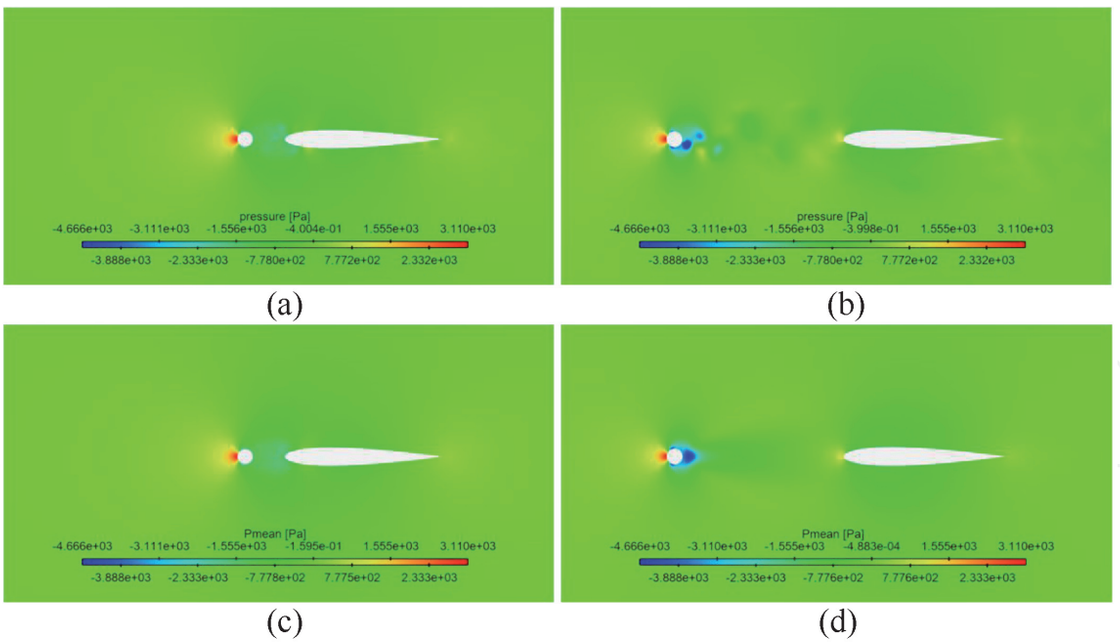

Figure 11.
Static pressure and mean pressure fields. (a) L/d = *2; (b)* L/d = *10; (c)* L/d = *2; (d)* L/d = *10.*

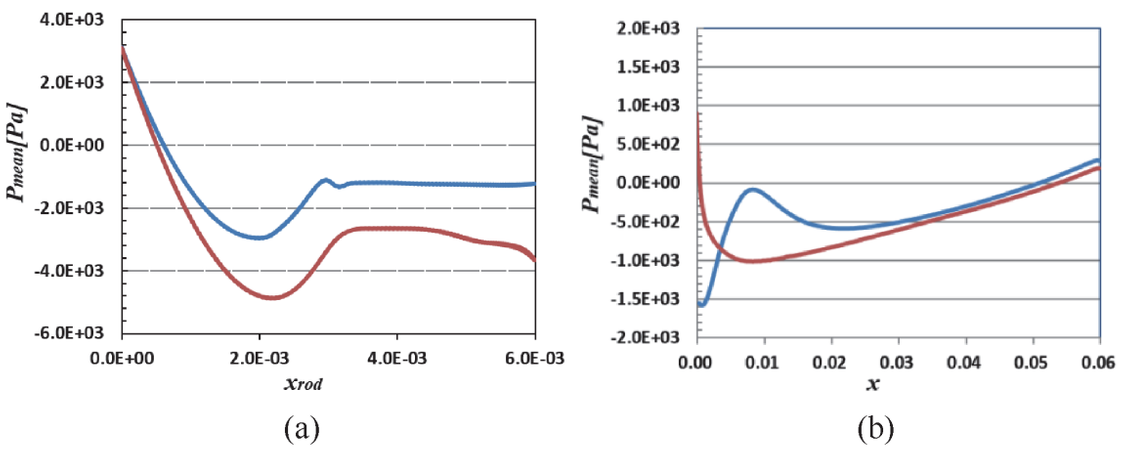

Figure 12.
Mean pressure profile on the rod and the airfoil. (a) Rod. (b) Airfoil. —— L/d = *2;* —— L/d = *10.*

the case of L/d = 2, as shown in **Figure 12(a)**, the pressure behind the rod is much larger than that for the case of L/d = 10 due to the presence of the airfoil behind the rod. As mentioned in Section 3.1.1, this phenomenon is related to the reattachments of the separated shear layers from the rod to the leading edge of the airfoil, and the Kármán-vortex street formed from the rod is suppressed and the pressure behind the rod increases. **Figure 12(b)** shows that in the case of L/d = 2, the negative pressure occurs around the leading edge of the airfoil, which means that the negative drag force acts on the airfoil, and in the case of L/d = 10, the positive pressure occurs the leading edge of the airfoil and the influence of the rod on the airfoil seems to be small.

Figure 13 shows instantaneous snapshots of a fluctuation pressure (dp) and RMS of the fluctuation pressure (dp_{rms}) fields, and the fluctuation pressure is defined as follows [6].

$$dp = p_s - p_{\text{mean}} \tag{12}$$

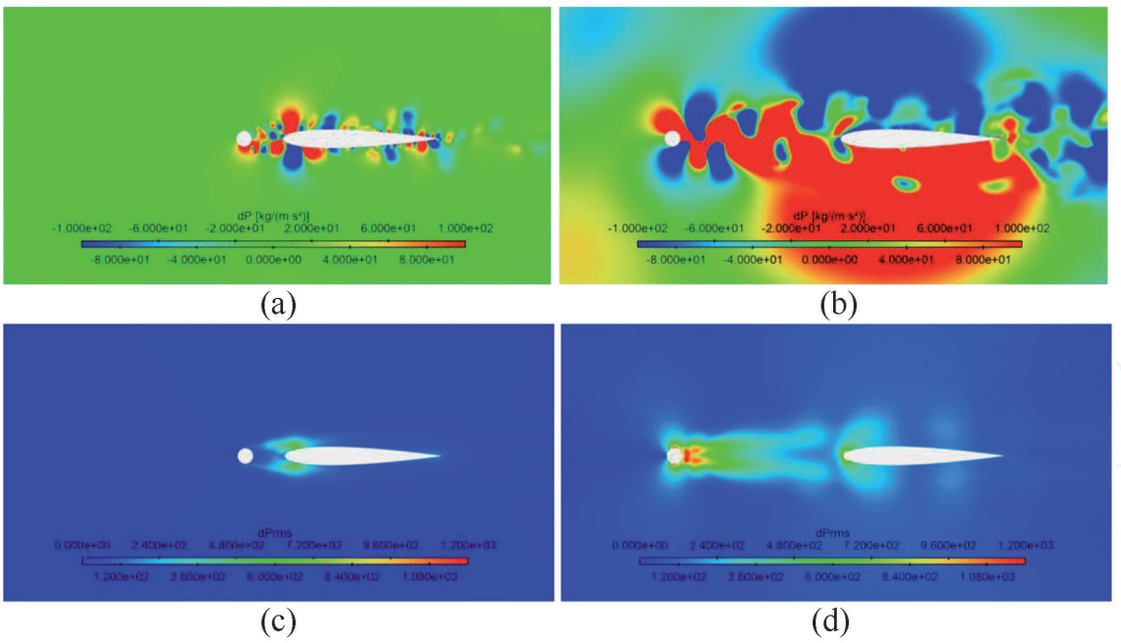

Figure 13.
Fluctuation pressure and RMS of fluctuation pressure fields. (a), (b) Fluctuation pressure, (c), (d) RMS of fluctuation pressure. (a) L/d = *2; (b)* L/d = *10; (c)* L/d = *2; (d)* L/d = *10.*

Here, p_s is the static pressure and p_{mean} is the mean pressure as represented in **Figure 11(c)** and **(d)**. As shown in **Figure 13(a)** and **(b)**, in the case of L/d = 2, the pressure fluctuation mainly occurs around the leading edge of the airfoil, and the pressure fluctuation in the region near the rod is much lower than that near the leading edge of the airfoil. This result is related to the reattachment of the shear layers formed from the rod to the airfoil as mentioned in Section 3.1.1. **Figures 8(a), 13(a)** and **(c)** show that the suppression of the vortex shedding from the rod results in the suppression of the noise radiation from the rod-airfoil model, as mentioned by Munetaka et al. [10] and Jiang et al. [21].

On the other hand, in the case of L/d = 10, that is, for large spacing, the pressure fluctuation near both the rod and the leading edge of the airfoil is large, and especially the pressure fluctuation near the rod is larger than that near the leading edge of the airfoil, as shown in **Figure 13(b)** and **(d)**. **Figures 8(b), 13(b)** and **(d)** show that the pressure fluctuation behind the rod is generated by the vortex shedding from the rod. They also show that the pressure fluctuation near the leading edge of the airfoil is generated by the impingement of the vortices shed from the rod onto the leading edge of the airfoil and the distortion of the impinged vortices (wake-body interaction or body-vortex interaction), as mentioned by Boudet et al. [16]. Similar phenomenon is investigated by Inoue and Mori [6] in the simulations of the noise generated by the flow around two square cylinders in tandem. They reported that the distortion of the impinging vortices shed from the upstream cylinder onto the downstream cylinder plays an important role for the noise radiation when the spacing between the two cylinders is large [6].

The distributions of the mean pressure and RMS of the fluctuation pressure in the wake region of the rod along the symmetry line (y = 0) of the rod and the airfoil are represented in **Figure 14**. As shown in **Figure 14(a)**, in the case of L/d = 2, the mean pressure is negative in the wake region between the rod and the leading edge of the airfoil, and it leads to the negative drag of the airfoil as mentioned above. In the case of L/d = 10, the mean pressure behind the rod is negative and much lower than in the case of L/d = 2, and that near the leading edge of the airfoil is positive, which leads to the positive drag of the airfoil. **Figure 14(b)** shows that in the case of

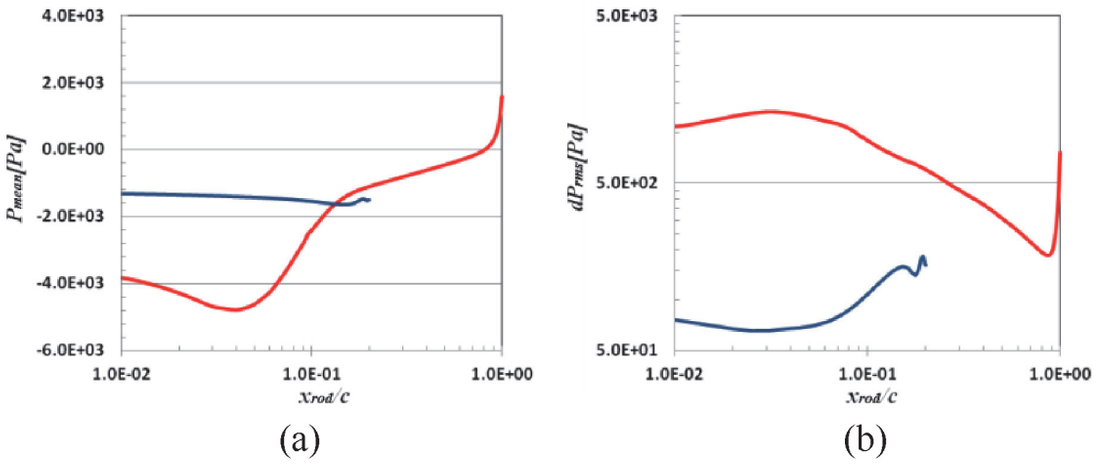

Figure 14.
Distributions of mean pressure and RMS of fluctuation pressure in wake region of rod along symmetry line (y = 0) of rod and airfoil. (a) Mean pressure (b) RMS of fluctuation pressure. —— L/d = 2; —— L/d = 10.

L/d = 2, the RMS of the fluctuation pressure in the region near the rod is much lower than that near the leading edge of the airfoil due to the suppression of the vortex shedding form the rod, and in the case of L/d = 10, the pressure fluctuation near both the rod and the leading edge of the airfoil is much larger than that in the case of L/d = 2 due to the vortex shedding from the rod and the impingement of the vortices on the leading edge of the airfoil, as mentioned in **Figure 13**.

4.1.3 Far acoustic pressure field

Figure 15 shows the spectra of the SPL at the location (x = 0.68 m, y = 1.74 m) calculated by the acoustic BEM simulation using the acoustic sources extracted from the CFD results. The SPL in the case of the single airfoil is also plotted to compare the two cases with it. The SPL in the case of L/d = 10 is much larger than that in the case of L/d = 2, and the peak frequencies for the cases of L/d = 10 and L/d = 2 are 2440 and 1960 Hz, respectively. However, the peak frequency for the case of L/d = 2 does not appear clearly compared to that in the case of L/d = 10, and the

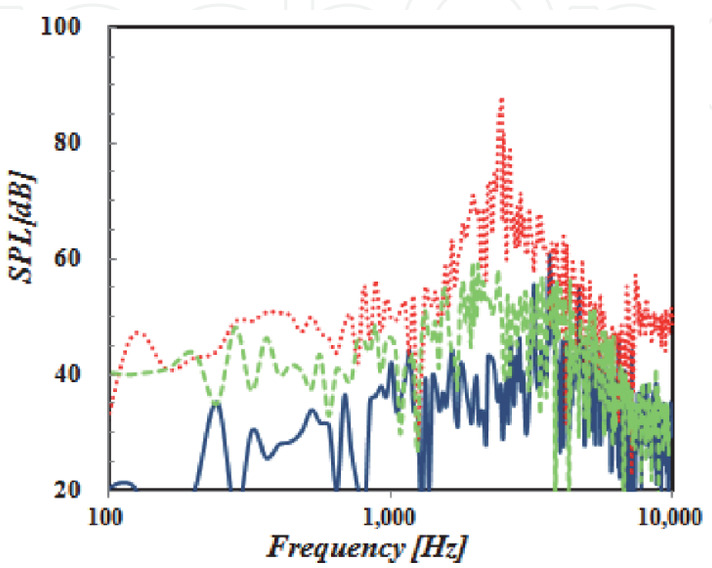

Figure 15.
SPL spectra at the location x = 0.68 *m,* y = 1.74 *m.* ····· L/d = 2; ····· L/d = 10; —— *single airfoil.*

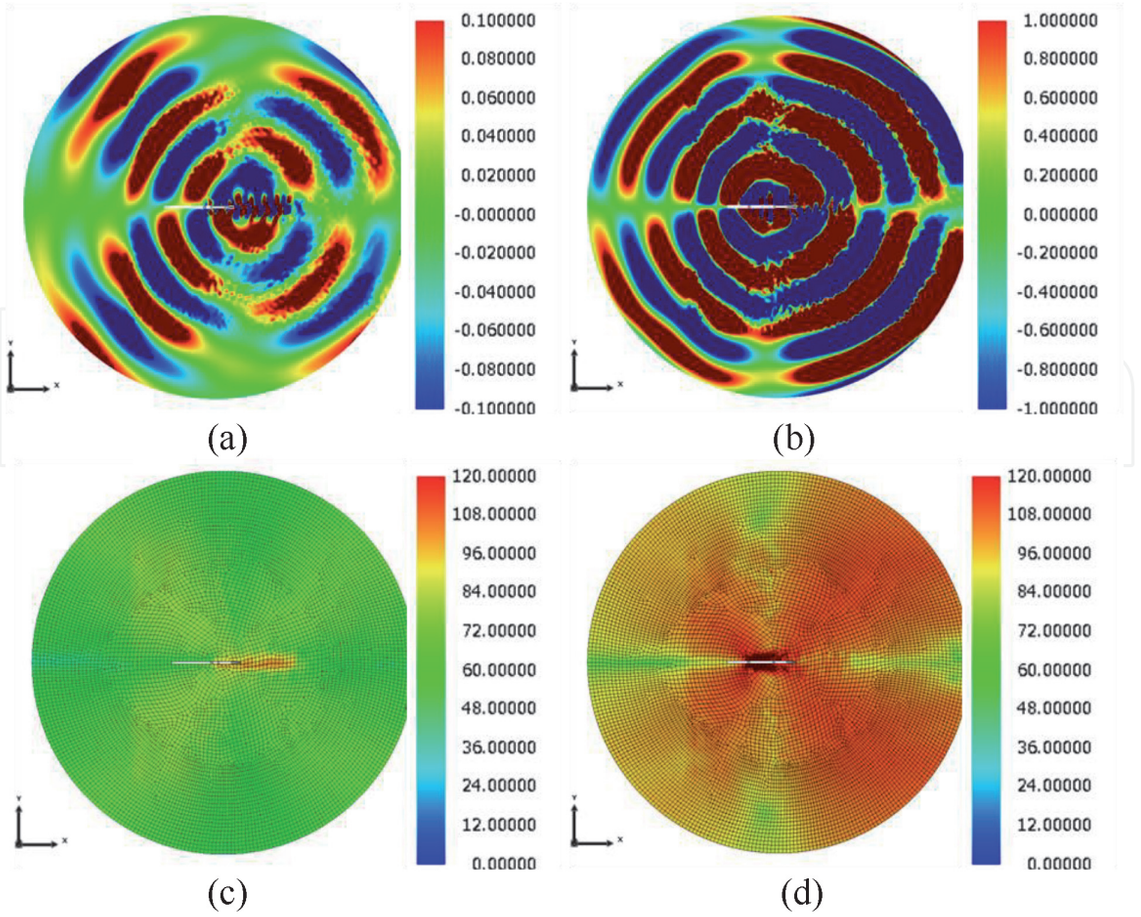

Figure 16.
Far-field sound pressure and SPL fields at the peak frequency. (a), (b) Sound pressure and (c), (d) SPL. (a) L/d = *2, 1960 Hz; (b)* L/d = *10, 2440 Hz; (c)* L/d = *2, 1960 Hz; (d)* L/d = *10, 2440 Hz.*

peak frequency increases depending on the spacing between the rod and airfoil as reported by Jiang et al. [21]. The peak SPL in the case of single airfoil is larger than that in the case of L/d = 2, and the peak frequency is higher than those in the cases of L/d = 2 and 10. The sound radiation is mainly generated by both the vortex shedding from the rod and the impingement of the vortices shed from the rod onto the leading edge of the airfoil in the case of L/d = 10, as indicated by Boudet et al. [16]. According to Jiang et al. [21], when $L/d \geq 4$, the vortex shedding from the rod and the impingement of the shed vortices onto the leading edge of the airfoil are the main generation sources of the noise radiation. As mentioned in Section 3.1.2, the suppression of the vortex shedding from the upstream rod results in the suppression of the pressure fluctuation in the region between the rod and the airfoil and the noise radiation for the case of L/d = 2.

Figure 16 presents the far-field sound pressure and SPL fields at the peak frequency. The far-field sound pressure and SPL fields show a dipolar nature of the sound radiation, and the lift dipole is dominant in the fields. The magnitude of the generated noise in the case of L/d = 10 is much larger than that in the case of L/d = 2, as indicated above. In the case of the L/d = 2, the noise propagation on the upstream side is larger than that on the downstream side. On the other hand, in the case of the L/d = 10, the noise propagation on the downstream side is larger than that in the upstream direction, which means that impingement of the vortices shed from the rod onto the leading edge of the airfoil, in other words, the wake body interaction is the main generation of the far filed noise radiation.

4.2 Airfoil-airfoil simulation results

4.2.1 Flow patterns

Typical examples of instantaneous vorticity fields are presented in **Figure 17**. In the present calculation, for the case of L/c = 0.2, when the spacing between the two airfoils is small, the boundary layers separated from the airfoil upstream did not roll up and reattach to the airfoil downstream. It seems that the reattached shear layers are oscillating at the leading edge of the downstream airfoil. The shear layers rolled up and formed vortices on the downstream airfoil surface, and the vortices were shed and convected downstream. On the other hand, in the cases of L/c = 0.6 and 1.0, the shear layers shed from the leading edge rolled up in front of the leading edge of the airfoil and impinged onto the leading edge of the airfoil. In the case of the single, the shear layer and the vortices shed only from the trailing edge of the airfoil.

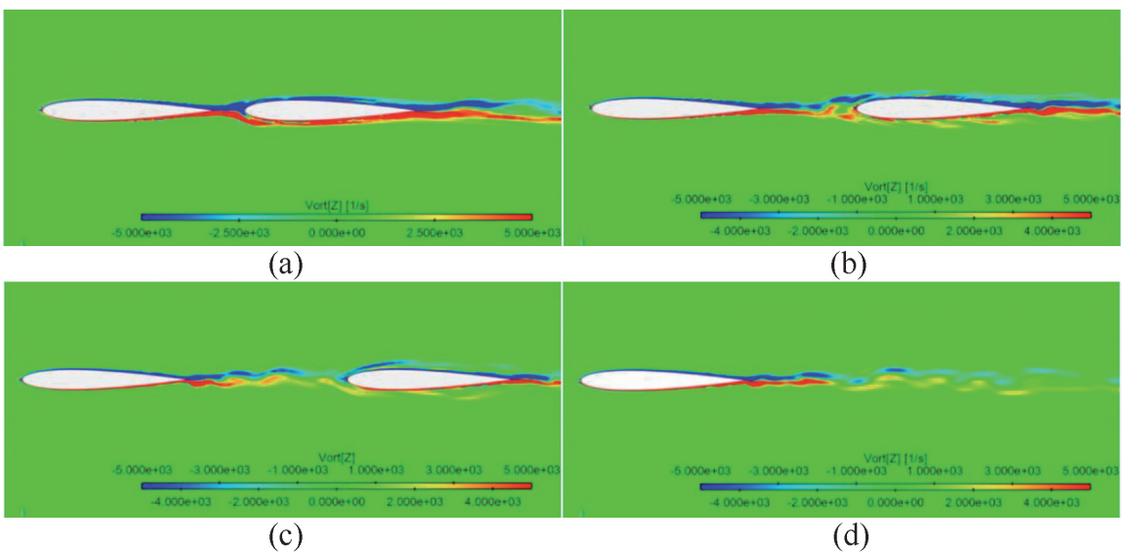

Figure 17.
Vorticity in the z *direction. (a)* L/c = *0.2; (b)* L/c = *0.6; (c)* L/c = *1; (d) single airfoil.*

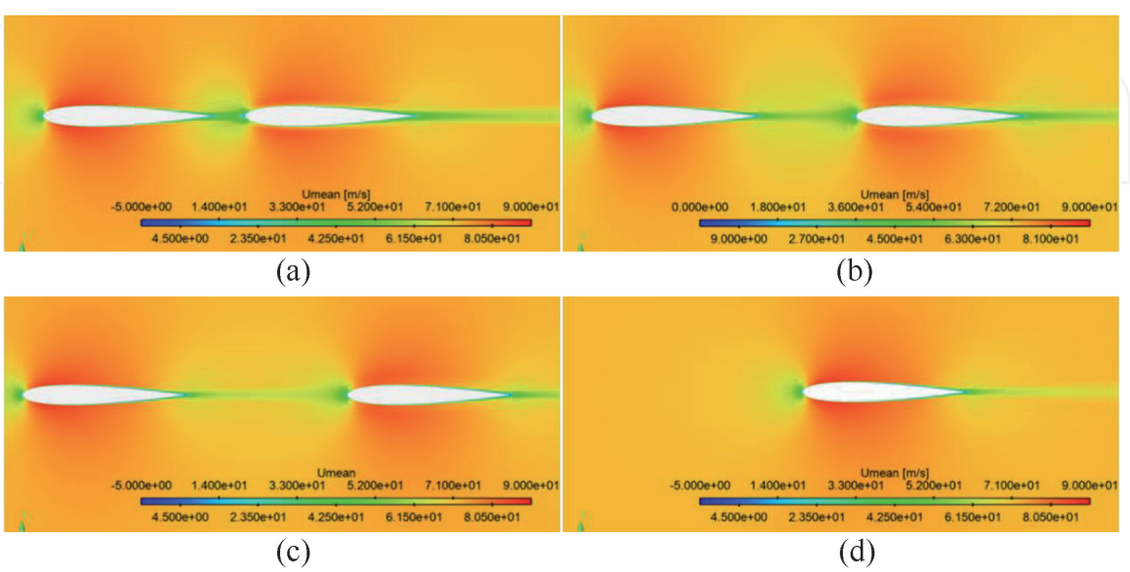

Figure 18.
Time-averaged velocity in the streamwise (x) *direction. (a)* L/c = *0.2; (b)* L/c = *0.6; (c)* L/c = *1; (d) single airfoil.*

Figure 18(a) and **(b)** show the fields of time-averaged velocity U_{mean} in the x (streamwise) direction. In the spacing between the two airfoils, **Figure 18(a)** shows that the shear layers shed from the upstream airfoil near the leading edge of the airfoil lead to very small or negative values of U_{mean} for the case of L/c = 0.2. The reattachments of the shear layer shed from the upstream airfoil to the leading edge of the airfoil due to the approaching airfoil slow down the flow. By contrast, for the cases of L/c = 0.6 and 1, the flow behind the upstream airfoil was accelerated in front of the leading edge of airfoil as shown in **Figure 18(b)** and **(c)**. These similar phenomena were observed in the rod-airfoil model, as explained in Section 3.1.1. In the case of the single, U_{mean} contour around the airfoil shows similar one of the two airfoils in the case of L/c = 1. The influence of the wake from the upstream airfoil seems to become smaller with the spacing between the two airfoils increasing.

Figure 19 shows the fields of time-averaged velocity V_{mean} in the y (vertical) direction. For the case of L/c = 0.2, the V_{mean} around the leading edge of the

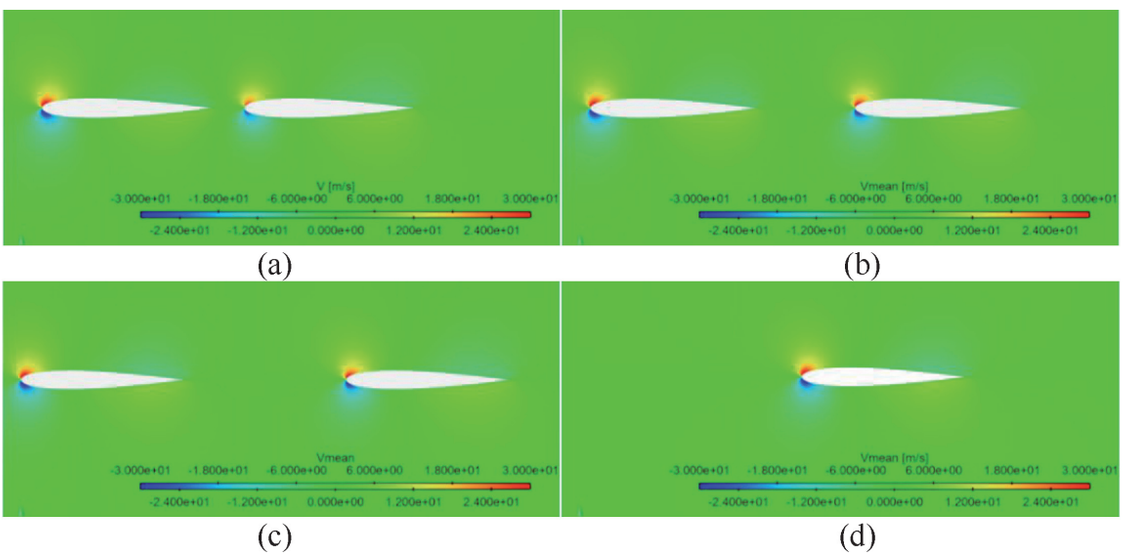

Figure 19.
Time-averaged velocity in the streamwise (x) *direction. (a)* L/c = *0.2; (b)* L/c = *0.6; (c)* L/c = *1; (d) single airfoil.*

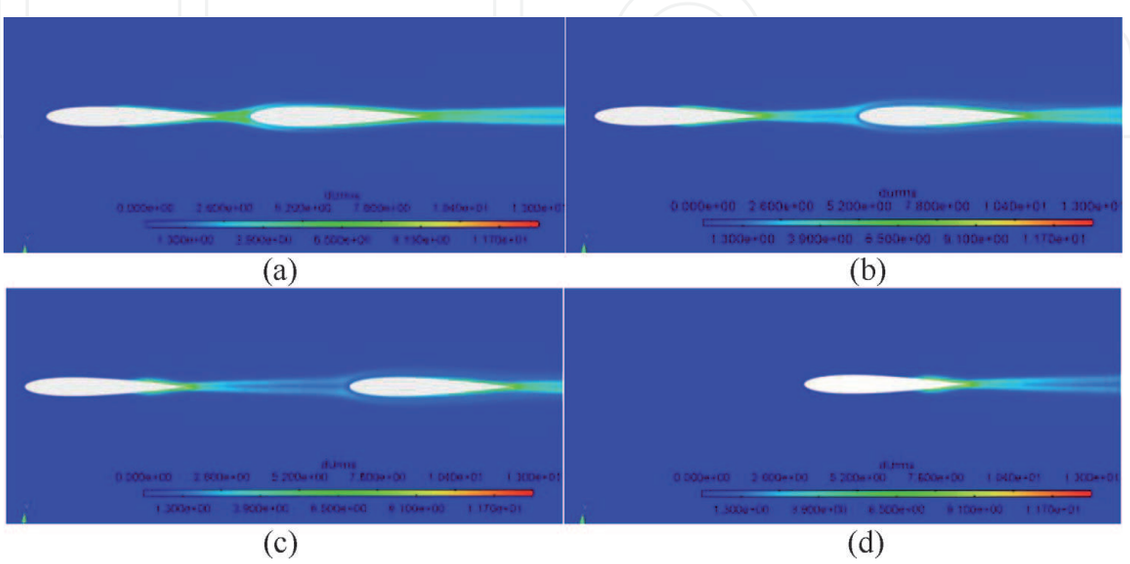

Figure 20.
RMS value of fluctuation velocity in the streamwise (x) *direction. (a)* L/c = *0.2; (b)* L/c = *0.6; (c)* L/c = *1; (d) single airfoil.*

downstream airfoil is lower than that in other cases. This is due to the reattachments of the shear layers shed from the upstream airfoil.

Finally, the fields of RMS value of the fluctuation velocity u_{rms} in the streamwise (x) direction are represented in **Figure 20**. As shown in **Figure 20**, for the case of L/c = 0.2, the u_{rms} values around the trailing edges of the two airfoils are lower than those for the cases of L/c = 0.6, 1.0 and the single airfoil. This result corresponds to the reattachment of the shear layers to the airfoil (see **Figure 17(a)**) in this case. Therefore the turbulent fluctuations around the trailing edges of the two airfoils in the cases of L/c = 0.6 and 1.0 seem to be larger than those for the case of L/c = 0.2.

4.2.2 Near pressure field

Snapshots of mean pressure are represented in **Figure 21**. For the case of L/c = 0.2, **Figure 21** shows that the value of the static pressure on the leading edge of

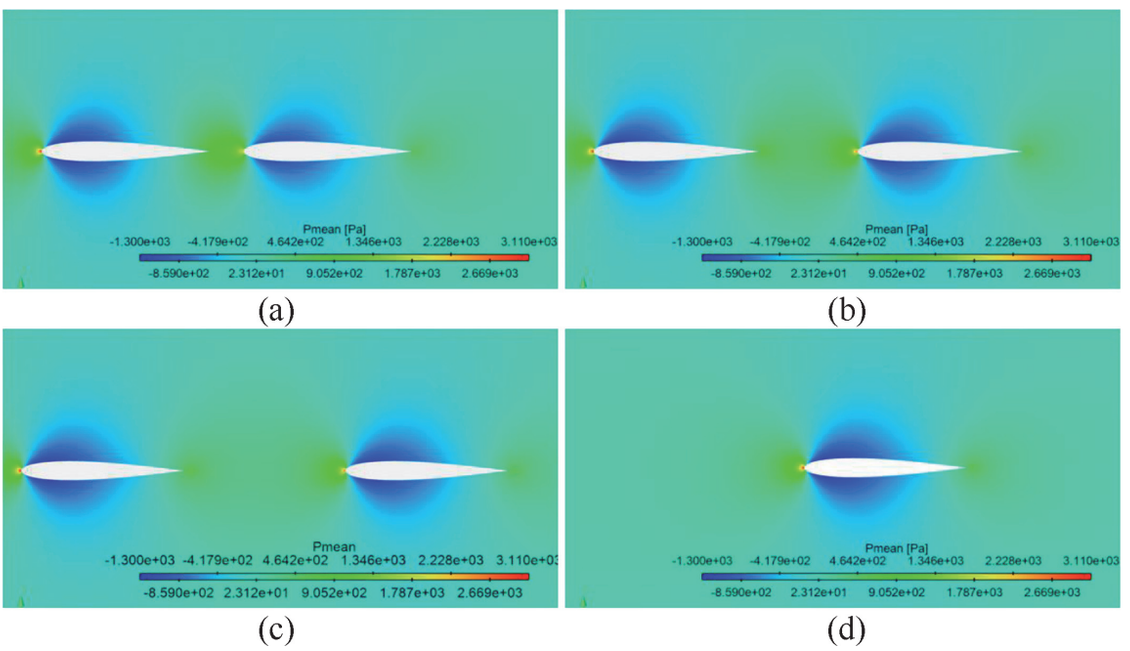

Figure 21.
Mean pressure field. (a) L/c = *0.2; (b)* L/c = *0.6; (c)* L/c = *1; (d) single airfoil.*

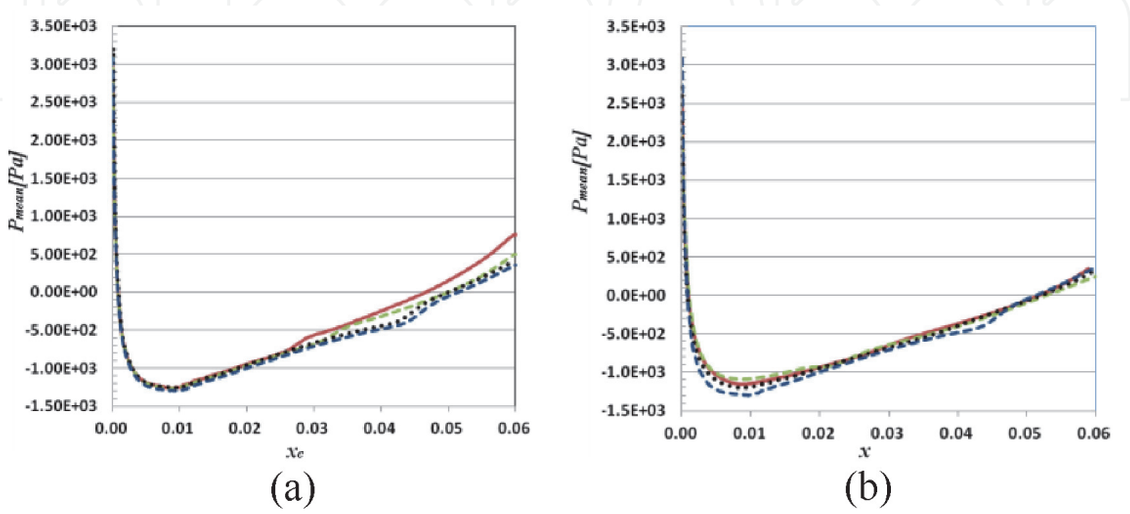

Figure 22.
Mean pressure profile on the upstream and downstream airfoils. (a) Upstream airfoil; (b) downstream airfoil.
L/c = *0.2;* ····· L/c = *0.6;* ····· L/c = *1.0;* - - - - *single airfoil.*

the upstream airfoil is much larger than that of the downstream one, and that on the leading edge of the downstream airfoil is much lower than those for the cases of L/c = 0.6, 1.0 and the single airfoil.

Figure 22 shows the mean pressure distribution on the surfaces of the two airfoils, where x_c is the coordinate in the streamwise direction and the origin of x_c is the located in the leading edge of the upstream airfoil. Depending on the spacing between the upstream and downstream airfoils, the pressure behind the upstream airfoil is affected by the downstream one. For the case of L/c = 0.2, as shown in **Figure 22(a)**, the pressure behind the upstream airfoil is larger than that for the cases of L/c = 0.6, 1 and single airfoil due to the presence of the downstream airfoil behind the upstream one. As mentioned in Section 3.2.1, this phenomenon is related to the reattachments of the separated shear layers from the upstream airfoil to the leading edge of the downstream airfoil, and the vortices formed from the upstream

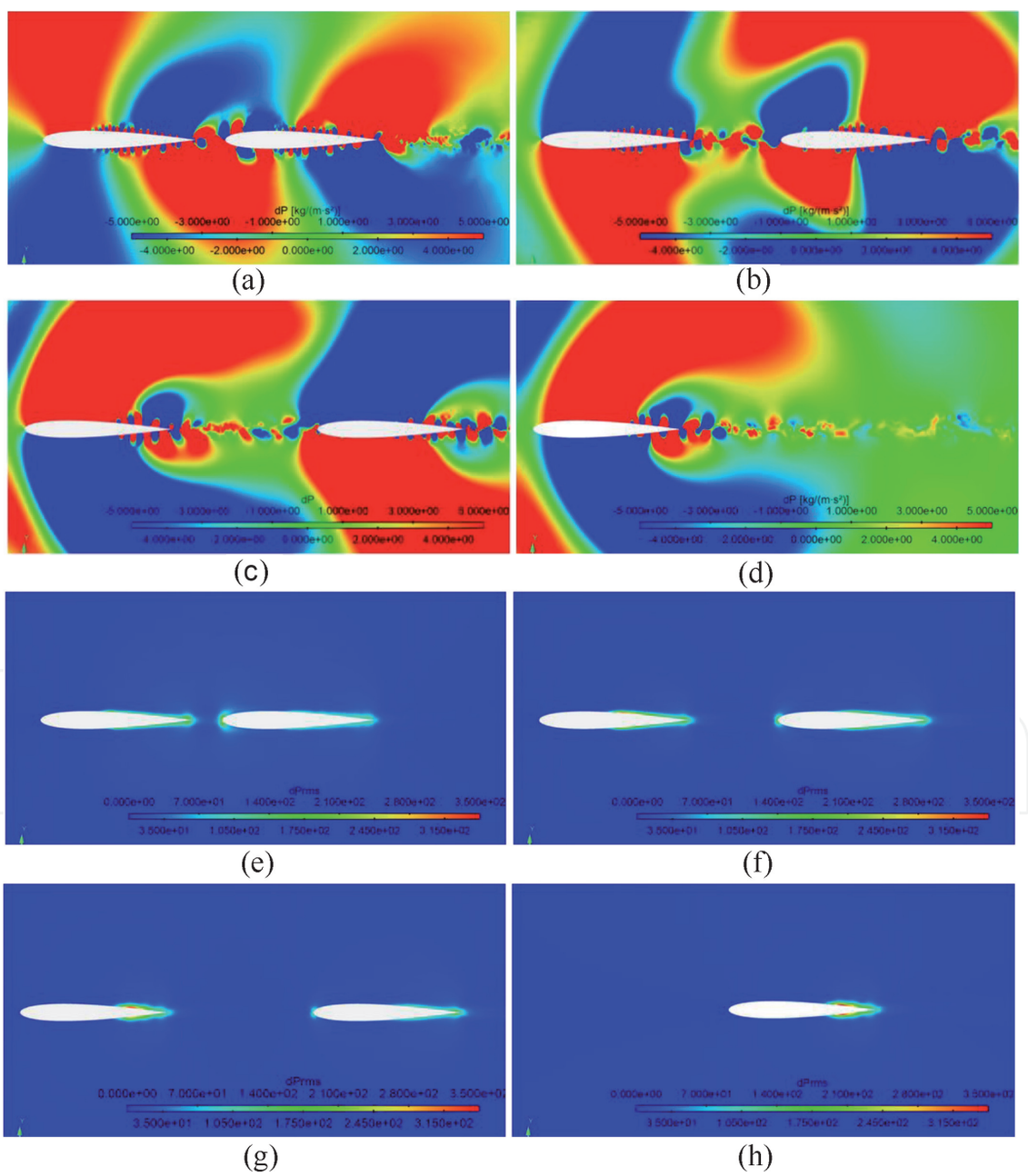

Figure 23.
Fluctuation pressure and RMS of fluctuation pressure fields. (a)–(d) Fluctuation pressure; (e)–(h) RMS of fluctuation pressure. (a) L/c = *0.2; (b)* L/c = *0.6; (c)* L/c = *1; (d) single airfoil; (e)* L/c = *0.2; (f)* L/c = *0.6; (g)* L/c = *1.0; (h) single airfoil.*

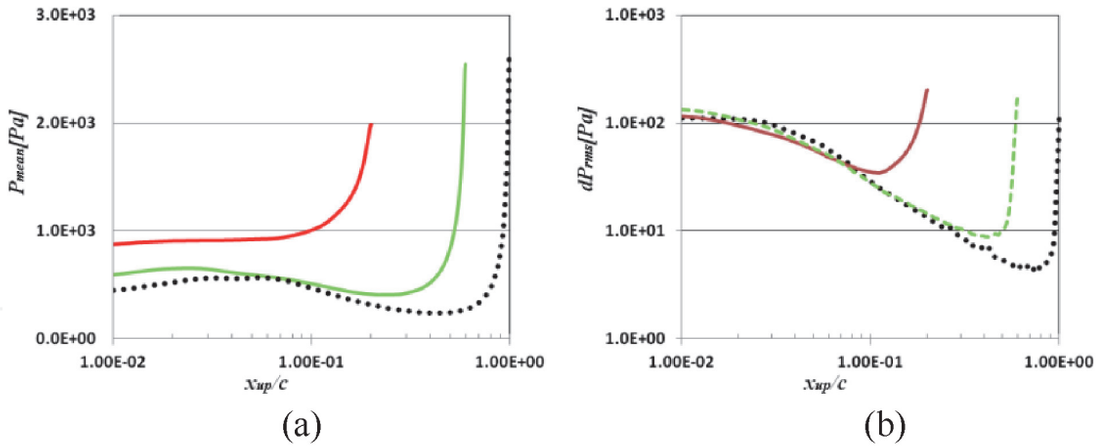

Figure 24.
Distributions of mean pressure and RMS of fluctuation pressure in wake region of upstream airfoil along symmetry line (y = 0) of two airfoils. (a) Mean pressure; (b) RMS of fluctuation pressure. —— L/c = *0.2;* – – – L/c = *0.6;* ····· L/c = *1.0.*

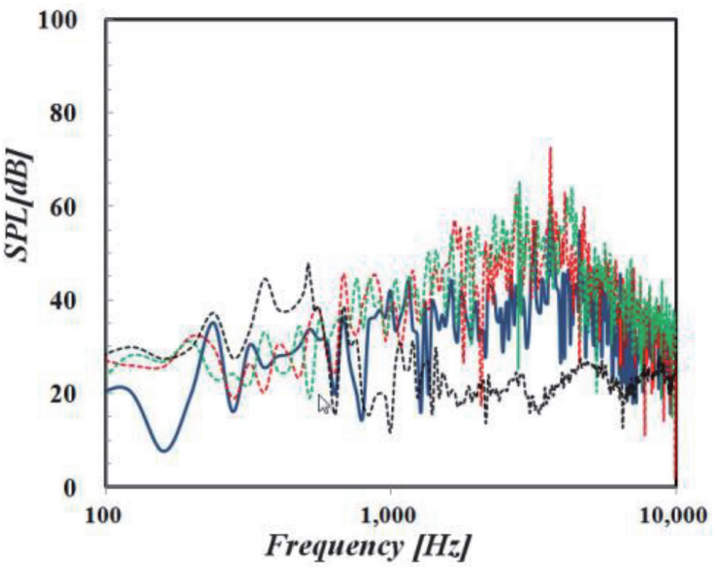

Figure 25.
SPL spectra at the location x = *0.68 m,* y = *1.74 m.* ····· L/c = *0.2;* ····· L/c = *0.6;* ····· L/c = *1.0;* —— *single airfoil.*

airfoil is suppressed and the pressure behind the upstream airfoil increases. **Figure 22(b)** shows that in the case of L/c = 0.2, the pressure around the leading edge of the downstream airfoil is lower than that in the cases of L/c = 0.6, 1 and single airfoil, which means that the drag force acting on the downstream airfoil is lower than that for the other cases.

Figure 23 shows instantaneous snapshots of a fluctuation pressure (dp) and snapshots of RMS of the fluctuation pressure (dp_{rms}) fields. As shown in **Figure 23 (a)–(c)**, in the two airfoil cases, the pressure fluctuation occurs around the trailing edge of the upstream airfoil and the leading and trailing edges of the downstream airfoil. In the case of single airfoil, the pressure fluctuation mainly occurs near the trailing edge of the airfoil as shown in **Figure 23(d)**. These figures show the dipolar nature of the fluctuation pressure generated around the trailing edge of the upstream airfoil and the leading and trailing edges of the downstream airfoil.

Figure 23(e)–(g) shows that the pressure fluctuation near the leading edge of the downstream airfoil is generated by the impingement of the shear layers or

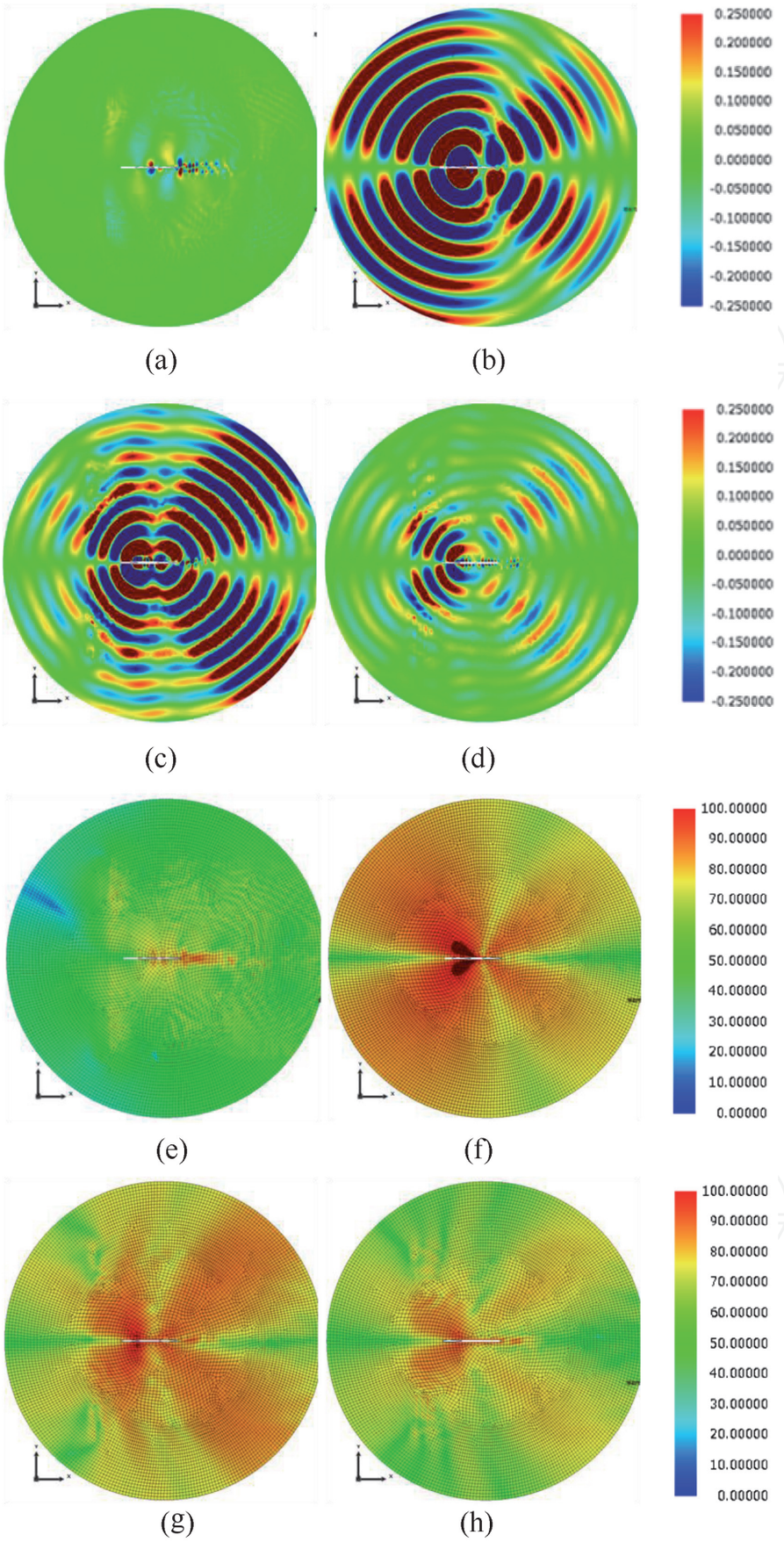

Figure 26.
Far-field sound pressure and SPL fields at the peak frequency. (a)–(d) Sound pressure and (e)–(h) SPL. (a) L/c = 0.2; *(b)* L/c = 0.6; *(c)* L/c = 1; *(d) single airfoil; (e)* L/c = 0.2; *(f)* L/c = 0.6; *(g)* L/c = 1.0; *(h) single airfoil.*

vortices shed from the upstream airfoil onto the leading edge of the downstream airfoil and the distortion of the impinged vortices (wake-body interaction or body-vortex interaction), as mentioned in Section 3.1.2.

The distributions of the mean pressure and RMS of the fluctuation pressure in the wake region of the upstream airfoil along the symmetry line ($y = 0$) of the two airfoils are represented in **Figure 24**. As shown in **Figure 24(a)**, the mean pressure behind the upstream airfoil is positive and lower than that near the leading edge of the downstream airfoil, and it decreases depending on the spacing between the two airfoils. On the other hand, that near the leading edge of the downstream airfoil increases depending on the spacing between the two airfoils. **Figure 24(b)** shows that the pressure fluctuation near both the trailing edge of the upstream airfoil and the leading edge of the downstream airfoil is large due to the shear layers or vortices shed from the upstream airfoil and the impingement of the shear layers or vortices onto the leading edge of the downstream airfoil, as mentioned in **Figure 23**.

4.2.3 Far acoustic pressure field

Figure 25 shows the spectra of the SPL at the location ($x = 0.68$ m, $y = 1.74$ m) calculated by the acoustic BEM simulation using the acoustic sources extracted from the CFD results. The SPL in the case of the single airfoil is also plotted to compare the three cases with it. The SPLs in the cases of $L/c = 0.6$, 1.0 and single airfoil are much larger than that in the case of $L/c = 0.2$, and the peak frequencies for the cases of $L/c = 0.2$, 0.6, 1.0 and single airfoil are 540, 2840, 3640, and 3640 Hz, respectively. **Figure 26** shows the far field sound pressure and SPL fields at the peak frequency. The peak frequency increases depending on the spacing between the two airfoils as reported in the rod-airfoil model. The peak SPL in the case of single airfoil is larger than that in the case of $L/c = 0.2$. The peak frequency in the case of the single airfoil is higher than those in the cases of $L/c = 0.2$ and 0.6, and same as that in the case of $L/c = 1.0$.

In the cases of the two airfoils, the sound radiation is mainly generated by three factors: (1) vortices or shear layers shedding from the upstream airfoil, (2) the impingement of the vortices or shear layers shed from the upstream airfoil onto the leading edge of the downstream airfoil, (3) vortices or shear layers shedding from the downstream airfoil as indicated in Section 3.2.2. As mentioned in Section 3.2.2, the reattachment of the shear layers from the upstream airfoil to the leading edge of the downstream airfoil results in the suppression of the pressure fluctuation in the region between the upstream and downstream airfoils and the noise radiation for the case of $L/c = 0.2$.

5. Conclusions

In this chapter, we simulated the flow around the rod-airfoil model and the noise generated by the wake-body interaction or body-vortex interaction by the coupling method using commercial CFD and acoustic BEM codes, and compared the results with those obtained by Jacob et al. [9] and Jiang et al. [21]. Then, we simulated the flow around the airfoil-airfoil model (airfoils in tandem) and the noise generation and propagation.

1. In the rod-airfoil model, when the spacing between the rod and the airfoil is small, the shear layers separated from the rod upstream did not roll up and

reattach to the airfoil downstream, and the vortex shedding from the rod is suppressed. It leads to the suppression of the pressure fluctuation near the rod and the airfoil and the noise radiation as reported by Jiang et al. [21].

2. In the rod-airfoil model, when the spacing between the rod and the airfoil is large, the boundary layers separated from the rod upstream rolled up and formed vortices, and the formed vortices shed from the rod impinged on the leading edge of the airfoil. This phenomenon is called the wake-body interaction or body-vortex interaction. It leads to the large pressure fluctuation near both the rod and the leading edge of the airfoil and the large noise radiation.

3. In the airfoil-airfoil model, the flow depends on the spacing between the two airfoils as in the rod-airfoil model. The shear layers shed from the upstream airfoil reattaches to the leading edge of the downstream airfoil with the small spacing between the two airfoils, and the reattached shear layers seem to oscillate at the leading edge of the downstream airfoil. The shear layers shed from the leading edge rolled up in front of the leading edge of the airfoil and impinged onto the leading edge of the airfoil with the large spacing between the two airfoils.

4. In the airfoil-airfoil model, the sound radiation is mainly generated by three factors: (1) vortices or shear layers shedding from the upstream airfoil, (2) the impingement of the vortices or shear layers shed from the upstream airfoil onto the leading edge of the downstream airfoil (the wake-body interaction), (3) vortices or shear layers shedding from the downstream airfoil as in the rod-airfoil model. The SPL and the peak frequency of the generated noise increase with an increase of the spacing between the two airfoils as reported in the rod-airfoil model.

Author details

Masaaki Mori
Cybernet Systems Co., Ltd., Tokyo, Japan

*Address all correspondence to: m-mori@cybernet.co.jp

References

[1] Mahir N, Rockwell D. Vortex shedding from a forced system of two cylinders. Part I: Tandem arrangement. Journal of Fluids and Structures. 1996;**9**: 473-489

[2] Zdravkovich MM. Review of flow interference between two circular cylinders in various arrangements. Journal of Fluids Engineering. 1977;**99**: 618-633

[3] Ljungkrona L, Norberg CH, Sunden B. Free-stream turbulence and tube spacing effects on surface pressure fluctuations for two tubes in an in-line arrangement. Journal of Fluids and Structures. 1991;**5**:701-727

[4] Liu CH, Chen JM. Observations of hysteresis in flow around two square cylinders in a tandem arrangement. Journal of Wind Engineering and Industrial Aerodynamics. 2002;**90**(9): 1019-1050

[5] Fitzpatrick JA. Flow/acoustic interactions of two cylinders in cross-flow. Journal of Fluids and Structures. 2003;**17**:97-113

[6] Inoue O, Mori M, Hatakeyama N. Aeolian tones radiated from flow past two square cylinders in tandem. Physics of Fluids. 2006;**18**:046101

[7] King WFN, Pfizenmaier E. An experimental study of sound generated by flows around cylinders of different cross-section. Journal of Sound and Vibration. 2009;**328**:318-337

[8] Hutcheson FV, Brooks TF. Noise radiation from single and multiple rod configurations. International Journal of Aeroacoustics. 2012;**11**:291-334

[9] Jacob MC, Boudet J, Casalino D, Michard M. A rod–airfoil experiment as benchmark for broadband noise modeling. Theoretical and Computational Fluid Dynamics. 2005; **19**(3):171-196

[10] Munekata M, Kawahara K, Udo T, Yoshikawa H, Ohba H. An experimental study on aerodynamic sound generated from wake interference of circular cylinder and airfoil vane in tandem. Journal of Thermal Science. 2006;**15**(4): 342-348

[11] Munekata M, Koshiishi R, Yoshikawa H, Ohba H. An experimental study on aerodynamic sound generated from wake interaction of circular cylinder and airfoil with attack angle in tandem. Journal of Thermal Science. 2008;**17**(3):212-217

[12] Li Y, Wang XN, Chen ZW, Li ZC. Experimental study of vortex-structure interaction noise radiated from rod–airfoil configurations. Journal of Fluids and Structures. 2014;**51**(3):313-325

[13] Casalino D, Jacob MC, Roger M. Prediction of rod airfoil interaction noise using the FWH analogy. AIAA Journal. 2003;**41**(2):182-191

[14] Jiang M, Li XD, Zhou JJ. Experimental and numerical investigation on sound generation from airfoil-flow interaction. Applied Mathematics and Mechanics. 2011; **32**(6):765-776

[15] Magagnato F, Sorgüven E, Gabi M. Far field noise prediction by large eddy simulation and Ffowcs-Williams Hawkings analogy. AIAA Journal. 2003; **6**:2003-3206

[16] Boudet J, Grosjean N, Jacob MC. Wake-airfoil interaction as broadband noise source: A large-eddy simulation study. International Journal of Aeroacoustics. 2005;**4**(1):93-116

[17] Greschner B, Thiele F, Jacob MC, Casalino D. Prediction of sound

generated by a rod–airfoil configuration using EASM DES and the generalised Lighthill/FW-H analogy. Computers and Fluids. 2008;**37**:402-413

[18] Agrawal BR, Sharma A. Aerodynamic noise prediction for a rod–airfoil configuration using large eddy simulations. AIAA Journal. 2014;**6**: 2014-3295

[19] Giret JC, Sengissen A, Moreau S, Sanjosé M, Jouhaud JC. Noise source analysis of a rod–airfoil configuration using unstructured large eddy simulation. AIAA Journal. 2015;**53**(4): 1062-1077

[20] Daude F, Berland J, Emmert T, Lafon P, Crouzet F, Bailly C. A high-order finite-difference algorithm for direct computation of aerodynamic sound. Computers and Fluids. 2012;**61**: 46-63

[21] Jiang Y, Mao ML, Deng XG, Liu HY. Numerical investigation on body-wake interaction over rod-airfoil configuration. Journal of Fluid Mechanics. 2015;**779**:1-35

[22] Xiao L, Syamir ASA, Mahdi A. Noise control for a tandem airfoil configuration using trailing edge serration. In: Proceedings of the 24th International Congress on Sound and Vibration (ICSV24). London; 2017. pp. 23-27

[23] Xiao L, Syamir ASA, Mahdi A, Yannick M. Aeroacoustic and aerodynamic study of trailing-edge serrated airfoils in tandem configuration. In: Proceedings of the 23rd International Congress on Acoustics (ICA23). Aachen; 2019. pp. 9-13

[24] Lighthill MJ. On sound generated aerodynamically. I. General theory. Proceedings of the Royal Society A: Mathematical, Physical and Engineering Sciences. 1952;**211**(1107):564-587

[25] Lighthill MJ. On sound generated aerodynamically. II. Turbulence as a source of sound. Proceedings of the Royal Society A: Mathematical, Physical and Engineering Sciences. 1954; **222**(1148):1-32

[26] Zhan T, Zhang Y, Ouyang H. Structural vibration and fluid borne noise induced by turbulent flow through a 90° piping elbow with/without a guide vane. International Journal of Pressure Vessels and Piping. 2015;**125**:66-77

[27] Zhang Y, Zhang T, Ouyang H, Li TY. Flow-induced noise analysis for 3D trash rack based on LES/Lighthill hybrid method. Applied Acoustics. 2014;**77**:141-152

[28] Mori M, Masumoto T, Ishihara K. Study on acoustic and flow induced noise characteristics of T-shaped pipe with square cross-section. Advances in Applied Acoustics. 2016;**5**:6-17

[29] Croaker P, Kinns R, Nicole K, Marburg S. Fast low-storage method for evaluating Lighthill's volume Quadrupoles. AIAA Journal. 2013;**51**(4): 867-884

[30] Mori M, Masumoto T, Ishihara K. Study on acoustic, vibration and flow induced noise characteristics of T-shaped pipe with a square cross-section. Advances in Applied Acoustics. 2017;**5**: 10-17

[31] Pierce AD. Acoustics: An Introduction to its Physical Principles and Applications. New York: McGraw-Hill; 1981